

Weak antilocalization beyond the fully diffusive regime in $\text{Pb}_{1-x}\text{Sn}_x\text{Se}$ topological quantum wells

Jiashu Wang,¹ X. Liu,¹ C. Bunker,¹ L. Riney,¹ B. Qing^{1,2}, M. Zhukovsky,³ T. Orlova,⁴ S. Rouvimov^{3,4}, M. Dobrowolska,¹ J. Furdyna,¹ B.A. Assaf¹

¹ *Department of physics, University of Notre Dame, Notre Dame IN 46556*

² *School of Science, Xi'an Jiaotong University, Xi'an Shaanxi, 710049, China*

³ *Department of Electrical Engineering, University of Notre Dame, Notre Dame IN, 46556*

⁴ *Notre Dame Integrated Imaging Facility, University of Notre Dame IN, 46556*

Abstract. We report the measurements and analysis of weak antilocalization (WAL) in $\text{Pb}_{1-x}\text{Sn}_x\text{Se}$ topological quantum wells in a new regime where the elastic scattering length is larger than the magnetic length. We achieve this regime through the development of high-quality epitaxy and doping of topological crystalline insulator (TCI) quantum wells. We obtain elastic scattering lengths that exceeds 100nm and become comparable to the magnetic length. In this transport regime, the Hikami-Larkin-Nagaoka model is no longer valid. We employ the model of Wittmann and Schmid to extract the coherence time from the magnetoresistance. We find that despite our improved transport characteristics, the coherence time may be limited by scattering channels that are not strongly carrier dependent, such as electron-phonon or defect scattering.

Introduction

The Z_2 topological insulator class – discovered more than a decade ago – has delivered several exciting fundamental advances and promises applications in quantum computing and spintronics. Recently, a crystalline symmetry protected topological phase has been identified in the IV-VI $\text{Pb}_{1-x}\text{Sn}_x\text{Te}$ and $\text{Pb}_{1-x}\text{Sn}_x\text{Se}$ material class. The two systems have been shown to host four Dirac cones per surface.^{1,2,3} Crystalline symmetry and valley degeneracy in these materials were proposed to yield a quantum Hall ferroelectric and a quantum anomalous Hall effect with a high-Chern number.^{4,5,6} These research frontiers have remained unexplored. Their realization requires IV-VI topological quantum wells (QWs) with low carrier density and a controlled interface chemistry and band alignment (shown in Fig. 1(a,b)). Such single QWs are not readily available.

Most previous studies reporting transport measurements on TCIs have studied weak antilocalization (WAL) in SnTe, a material known to host carrier densities on the order of $10^{20}\text{cm}^{-3}/\text{Vs}$ and mobilities on the order to $10\text{-}100\text{cm}^2/\text{Vs}$.^{7,8,9,10} Trivial PbSe, PbTe and the ternary non-trivial $\text{Pb}_{1-x}\text{Sn}_x\text{Se}$ and $\text{Pb}_{1-x}\text{Sn}_x\text{Te}$ have been synthesized with superior quality in the form of bulk epilayers and heterostructures.^{11,12,13,14,15,16,17} However, there has not been any effort dedicated to the synthesis of high-quality single QWs of the non-trivial class of those materials. Thus, while WAL has been extensively studied in TIs and spin-orbit coupled systems, it remains underexplored in TCIs – especially in high mobility samples. WAL is a very useful tool to probe the properties of Dirac electrons,^{18,19,20,21} particularly the Berry phase and how it is impacted by different symmetry breaking perturbations.

Preview

This work reports the realization of single QWs of TCI $\text{Pb}_{0.7}\text{Sn}_{0.3}\text{Se}$ with carrier density lower than 10^{13}cm^{-3} and mobility exceeding $10000\text{cm}^2/\text{Vs}$. This improved quality allows us to reach a new quantum coherent regime where the elastic scattering length L_e exceeds the magnetic length ($L_B^2 = \hbar/2eB$) for $B < 0.1\text{T}$.

In this limit, the well-known Hikami-Larkin-Nagaoka (HLN) model²² is no longer valid. We thus implement a quantum coherent transport model developed by Wittman and Schmid (WS)²³ that remains valid beyond the fully diffusive regime to extract the inelastic scattering time τ_ϕ and the Thouless coherence length. We show that the HLN model tends to overestimate the Thouless length L_{th} when compared to the WS model, but still reliably captures its decay versus temperature. Importantly, both models indicate that while L_{Th} exceeds $1\mu m$ in low density QWs, its decay is also enhanced. Our results suggest that scattering channels that are not strongly carrier density dependent dominate electron decoherence in the IV-VI system. Most notably, electron-phonon or long-range electron-defect scattering play dominant role.

Experimental Results

Growth and characterization

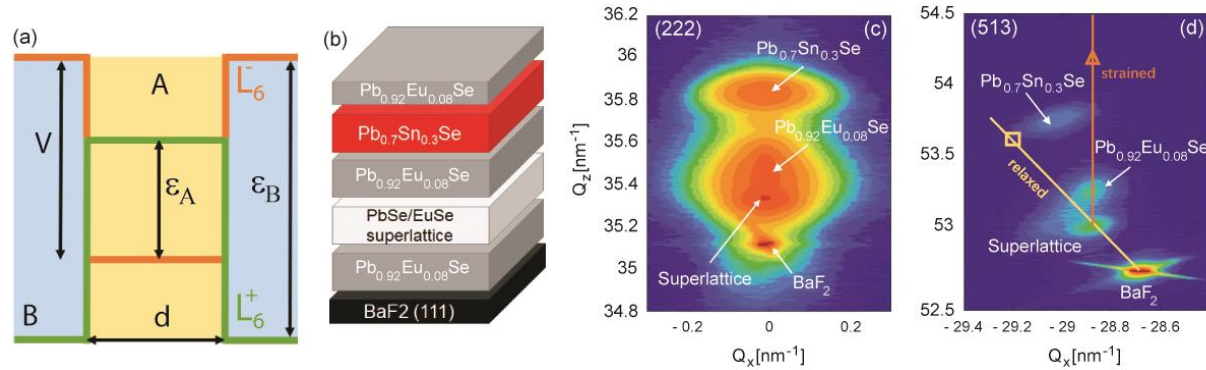


FIG 1. Basic properties for $Pb_{1-x}Sn_xSe$ (111) Quantum Well. (a) Energy diagram of the topological QW, showing the symmetric confinement potential and the inversion of the bulk conduction and valence bands in the well. $\epsilon_{A/B}$ denote the well (A) and barrier (B) energy gap respectively. V denotes the band offset at the interface and d is the thickness of the well. A band inversion occurs at the interfaces. (b) Structure diagram of quantum well. (c) X-ray diffraction reciprocal space map of (222) plane showing peaks attributed to the well, barrier, superlattice and substrate (d) RSM of (513) plane. It is clear that the superlattice is completely relaxed with respect to BaF_2 but it yields a slight in-plane tensile strain to $Pb_{0.7}Sn_{0.3}Se$. The expected fully relaxed and fully strained line of $Pb_{0.7}Sn_{0.3}Se$ are marked by \square , Δ respectively.

Quantum wells of $Pb_{1-x}Sn_xSe$ with $x \approx 0.3 \pm 0.03$ oriented in the (111) direction are grown by molecular beam epitaxy (MBE) on (111)- BaF_2 substrates. A buffer layer structure is utilized to reduce the lattice mismatch between the well ($a = 6.085 \text{ \AA}$) and the BaF_2 substrate ($a = 6.196 \text{ \AA}$). The buffer layer consists of a starting buffer layer of $Pb_{0.92}Eu_{0.08}Se$ (50nm, $a = 6.130 \text{ \AA}$) followed by a 50 short-period superlattice of $PbSe$ (1.6nm)/ $EuSe$ (1nm). The purpose of this initial structure is to suppress the propagation of lattice dislocations during growth and to maintain a smooth surface prior to the growth of the QW. A $Pb_{0.92}Eu_{0.08}Se$ barrier (45nm) is then grown on the superlattice followed by the $Pb_{0.7}Sn_{0.3}Se$ well ($55 \pm 5 \text{ nm}$) and a final capping layer $Pb_{0.92}Eu_{0.08}Se$ (35nm) is synthesized on top. A schematic of the structure is shown in Fig. 1(b).

High resolution X-ray diffraction is performed around the symmetric (222) node and the asymmetric (513) node. The resulting reciprocal space maps are shown in Fig. 1(c,d) respectively. Along the growth direction ($q_z \parallel (111)$), the Bragg peak resulting from the well is seen at the highest Bragg angle, clearly separated from the superlattice and buffer layer peaks. The $Pb_{0.7}Sn_{0.3}Se$ peak appears at an angle slightly higher than what is expected from the bulk lattice constant, suggesting that the layer maintains a slight residual lattice

strain that is tensile in the plane but compressive out-of-plane. The (513) space map shown in Fig. 1(d) confirms that while the buffer heterostructure is completely relaxed with respect to the BaF₂ substrate, the Pb_{1-x}Sn_xSe well is only partially relaxed with respect to the Pb_{0.9}Eu_{0.08}Se buffer and the superlattice. Bi doping is used to tune Fermi energy of the Pb_{1-x}Sn_xSe well, using an approach similar to what is already achieved in previous work.^{24,25} A series of four samples with varying Bi content are grown. Their characteristics are summarized in table 1.

| Sample | Bi cell temperature | Density [cm ⁻²] | Mobility[cm ² /Vs] | $L_e = v_F \tau_e$ | $B_{tr} = \frac{\hbar}{2eL_e^2}$ |
|--------|---------------------|-----------------------------|-------------------------------|--------------------|----------------------------------|
| QW-1 | No Bi | 3.6×10^{13} | 4130 | 80 nm | 530 Oe |
| QW-2 | 305°C | 3.1×10^{13} | 2950 | (52±4) nm | (1220±180) Oe |
| QW-3 | 310°C | -6.6×10^{12} | 11300 | 133 nm | 185 Oe |
| QW-4 | 320°C | -1.3×10^{13} | 8630 | (114±8) nm | (252±35) Oe |

Table 1. Sample information. From QW-1 to QW-4 we gradually increase the Bi doping density. The carrier density, mobility, mean free path and characteristic transport field are shown. They are all measured at 4.2K and found to not vary much between 4.2K and 10K.

Electrical transport measurements

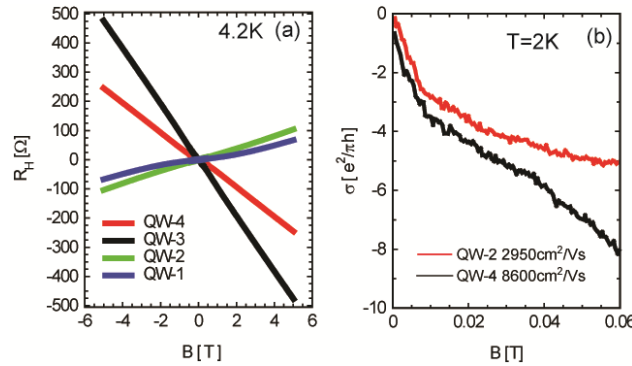


FIG 2. (a) Hall resistance of four QW with different Bi doping density. (b) Magnetoresistance at low field showing weak antilocalization effect in QW-2 and QW-4 at 2K.

Electrical Hall effect measurements performed on this sample series up to 5T and down to at 4.2K are shown in Fig. 2(a). A control sample of Pb_{0.9}Eu_{0.08}Se/(PbSe,EuSe)/Pb_{0.9}Eu_{0.08}Se is checked to confirm that the buffer heterostructure is electrically insulating. Its resistance is found to exceed 33MΩ at room temperature, four orders of magnitude higher than with the QW. Pristine Pb_{0.7}Sn_{0.3}Se is p-type with a Hall concentration close to 3.6×10^{13} cm⁻² likely due to group IV atom vacancies or substitutional defects. Bi is introduced into the lattice by co-evaporation during synthesis of the quantum well. Bi is a known donor in IV-VI materials and can alleviate defect-induced p-doping. The lowest 2D density that we reach is 6×10^{12} electrons/cm² with a mobility that is above 11000 cm²/Vs. Table 1 summarizes the carrier density and mobility (μ) extracted for four samples along with the corresponding elastic scattering length L_e and characteristic transport field B_{tr} . The computation of L_e requires a knowledge of the effective Fermi

velocity v_f and carrier effective mass m . Since the energy bands in IV-VI quantum wells are highly non-parabolic,^{26,17} both quantities depend on the Fermi energy. In Appendix A and B, we discuss our determination of those two quantities given that multiple QW subbands are occupied.^{27,28} After v_f and m are found, we have:

$$L_e = v_f \tau_e = \frac{v_f \mu m}{e}$$

The magnetoresistance of two samples (QW-2, QW-4) that this work will center on is shown in Fig. 2(b). A clear cusp is observed at low magnetic field. This cusp is characteristic of weak antilocalization (WAL) typically observed at low temperatures in materials with strong spin-orbit coupling^{29,30} including topological materials^{31,32,33}. It is due to the quantum interference of backscattered electron wavepackets that retain their coherence over multiple elastic scattering events.³⁴ The field dependence of the resistance due to WAL yields the coherence length (or time) of charge carriers in the system.

Modeling weak antilocalization

The well-known Hikami-Larkin-Nagaoka model^{22,35} (HLN) that describes the interference of electrons in the diffusive limit is used to extract the Thouless coherence length. At low magnetic fields, the quantum correction to the conductivity in this model is given by:

$$\Delta\sigma_{2D} = \frac{\alpha e^2}{\pi h} \left[\psi \left(\frac{\hbar}{4eBL_{th}^2} + \frac{1}{2} \right) - \ln \left(\frac{\hbar}{4eBL_{th}^2} \right) \right] + \beta B^2$$

$\alpha = 1/2$ per WAL channel. L_{th} is the Thouless coherence length and βB^2 is the term we add to account for cyclotronic magnetoresistance. $\alpha = 1/2$ per WAL channel (or Fermi surface). β is fixed independently to best fit the parabolic part of the magnetoconductivity at intermediate field.³⁵

We note that the HLN model is valid only if $L_{th} \ll L_e$ and if the applied field $B \ll B_{tr}$. For QW with high mobility such as QW-4, we find that $B_{tr} = 252$ Oe, of the same order of magnitude as the applied field. When $B \sim B_{tr}$, the number of collision events per trajectory approaches 1. We are likely at the limit of validity of the HLN model.^{22,36} In conjunction with this model, we utilize a model developed by Wittmann and Schmid²³ (WS) that remains valid beyond the diffusive regime, to independently extract the coherence time τ_ϕ . The WS model²³ is implemented by computing the quantum correction to conductivity from interfering electron wavepackets. In general, the quantum coherent correction to the conductivity is given by:²³

$$\Delta\sigma = -\frac{e^2}{\pi h} \sum_n F(b, n)$$

$F(b, n)$ is related the backscattering probability. In, the WS model,

$$\Delta\sigma(B) = -\frac{\alpha e^2}{\pi h(1 + \gamma^2)} \times \left[\sum_{n=0}^N \left(\frac{b \cdot \varphi_n^3(b)}{1 + \gamma - \varphi_n(b)} \right) - \ln \frac{1 + \gamma}{\gamma} \right] + \beta B^2$$

Where,

$$\gamma = \frac{\tau_e}{\tau_\phi} = \frac{L_e}{L_\phi}, \text{ and } b = \frac{B}{B_{tr}(1 + \gamma)^2} \quad \varphi_n(b) = \int_0^\infty dt e^{-t - \frac{bt^2}{4}} L_n(bt^2/2)$$

φ_n is the probability of a particle going back to the origin after $(n - 1)$ scattering events. L_n is the n -th Laguerre polynomial. Only two fit parameters are thus needed, α and γ . α has the same meaning as for HLN. γ yields the coherence time τ_ϕ . β is fixed to the same value used to fit the HLN model.

Previous work on III-V quantum wells have discussed a simplified implementation of the WS model.³⁶ At first sight the model seems to need a great amount of computational resources; we have used the approach discussed in ref³⁶ to optimize its implementation. Also note that, the WS model, has been used to interpret weak localization (WL) data in past. To implement it to analyze WAL, we have simply changed the sign of $\Delta\sigma$, since the quantum correction to conductivity is simply reversed in the case of WAL. Our approach is only likely to be off by a constant multiplicative factor. In other words, the extracted coherence time is expected to be reliable, however, α will likely not agree with that found using HLN. The next section of the paper shows the results and analysis obtained for two samples QW2 and QW4.

Comparison between the two models

Fig. 3(a) shows the curve fit by WS performed on the WAL cusp observed between 2K and 11K in QW-2. The fit parameters from the WS model are shown in Fig. 2(b). The coherence time increases with decreasing temperature up to 3K, indicating a decreasing inelastic scattering rate. A possible saturation is observed between 2K and 3K. A maximum coherence time close to 53ps is attained at 3K. Fig. 3(c) shows the same data analyzed using the HLN model. For QW-2, $B_{tr} = 1220$ Oe, the applied field is only half of that value, limiting the validity of the HLN model. The fit parameters are shown in Fig. 3(d). L_{th} reaches a maximum close to 880nm and then saturates. The behavior of L_{th} mirrors the decay of τ_ϕ as inelastic scattering is – as expected – enhanced with increasing temperature.

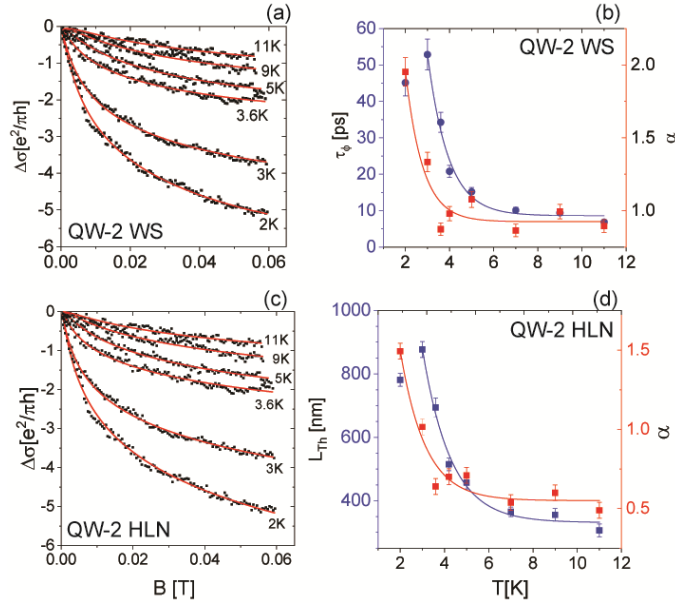


FIG 3. WAL analysis for QW-2. (a) WAL data at small field $<0.06T$ ($\approx 0.5B_{tr}$) from 2K to 10K. The solid red lines are the fitting curves obtained by the WS model and the points represent experimental data. (b) Fit

parameters obtained from WS fitting. (c) Same as (a) with the fitting curve obtained by the HLN model. (d) Fit parameters obtained from HLN. β is fixed at 0 for both WS and HLN. The lines in (b) and (d) are a guide for the eye.

Fig. 4 shows an identical analysis performed for QW-4 between 2K and 10K. Fig. 4(a) shows curve fits obtained using the WS model, up to 600Oe, with the resulting fit parameters shown in Fig. 4(b). The decay of τ_ϕ is again evident. A maximum that exceeds 100ps is obtained at 3K followed by a possible saturation. A curve fit using the HLN model is shown in Fig. 4(c), and the fit parameters are plotted in fig. 4(d). A similar enhancement of the coherence length is observed up to a possible maximum at 3K.

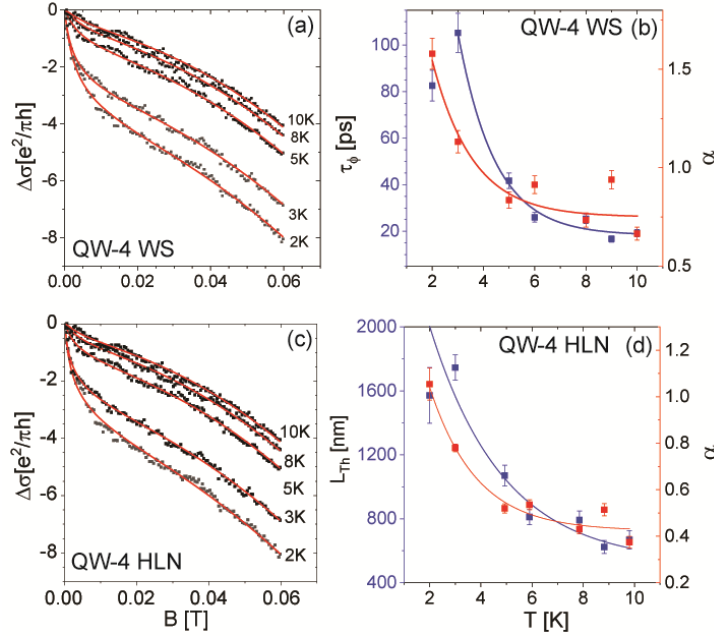


FIG 4. WAL analysis for QW-4. (a) WAL data at small field $<0.06T (\approx 2.4B_{tr})$ from 2K to 10K. The solid red lines are the fitting curves obtained by the WS model and the points represent experimental data. (b) Fit parameters obtained from WS fitting. (c) Same data as (a) with the fitting curve obtained by the HLN model. (d) Fit parameters obtained from HLN. β is fixed at $820 e^2/\pi h (\text{Tesla})^2$ for both WS and HLN. The lines in (b) and (d) are a guide for the eye.

In both QWs, α is seen to be strongly enhanced below 4K, suggesting that multiple transport channels start contributing WAL. While this is not the main focus of this work, it is worth noting that in our TCI QWs, in addition to valley degeneracy, multiple subbands can be occupied even at low density. The value of α can be a result of either. $\alpha = \frac{1}{2}$ per subband and per valley in the HLN model. If the inter-subband (valley) scattering time is longer than the coherence time, an independent contribution to WAL from each subband (valley) is observed and α is larger. The fact that α is larger in QW-2, regardless of model, suggests that the contribution of several independent trivial and non-trivial subbands likely causes the enhancement below 4K.

The disagreement between the two values of α recovered from the two models (Fig. 3(b) compared to 3(d) and Fig. 4(b) compared to 4(d)) is expected as discussed earlier and mentioned by Wittmann and

Schmid in their work.²³ Further theoretical insight is needed to truly understand how the numerical value of α per valley is altered beyond the work of Wittman and Schmid. Theoretical calculations considering WL in this limit suggest that non-backscattering contributions to $\Delta\sigma$ may need to be considered especially if $B \sim B_{tr}$.³⁷ At this point, it is evident that only L_{Th} and τ_ϕ merit further attention, as the determination of α from WS cannot be made reliably without a more in-depth theoretical treatment that includes spin-orbit coupling, spin-momentum locking, or non-backscattering contributions.

Dephasing rate versus temperature

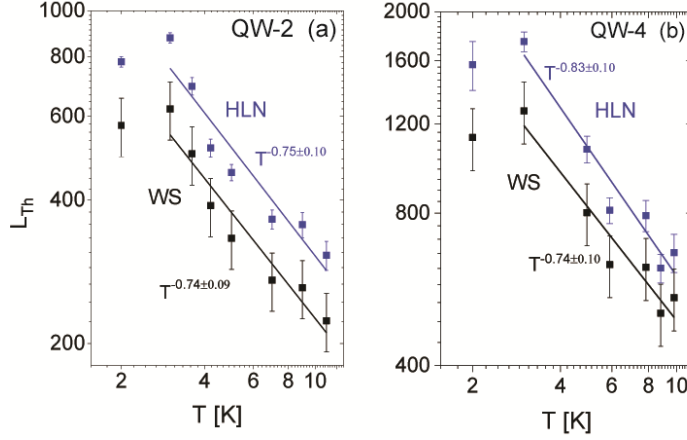


FIG 5. Coherence length L_{Th} as a function of temperature obtained from each model for QW-2 (a) and QW-4 (b) by fitting up to $0.06T$. The uncertainty on L_{Th} in the WS model is dominated by the uncertainty on the diffusion constant discussed in appendix B.

In Fig. 5(a,b), the coherence length $L_{th} = \sqrt{D\tau_\phi}$ extracted from WS is plotted in comparison with that obtained from HLN model. The Thouless length extract from WS is at least 30% lower than what is found using HLN. The result from HLN is consistently outside the error estimated (see appendix B) for the WS fit parameters. In both QWs, the lack of agreement likely results from B being comparable to B_{tr} . Regardless of the model used, a power law decay is obtained such that $L_{th} \sim T^{-p}$ with $p \approx 0.7 \sim 0.8$. We conclude that with the improvement of sample quality we approach the limit of validity of models that assume fully diffusive transport ($L_e \ll L_{th}$ or $B < B_{tr}$) in topological systems, such as the HLN model. In this limit, the extracted value of L_{th} is not reliable, however its decay versus temperature still agrees with WS model.

A decay exponent $p \approx 0.7 \sim 0.8$ in a QW suggests the coexistence of multiple dephasing mechanisms. In most 2D systems, $p = 0.5$ is found. It is explained by the work of Altshuler et al. that links decoherence at low temperature to Nyquist noise from the carrier bath impacting the single particle:^{38,39}

$$\tau_\phi^{-1} = \frac{D}{L_{Th}^2} \sim \frac{k_B T}{2\pi N D \hbar^2} \ln(\pi N D \hbar)$$

Electron-phonon scattering^{40,41,34} and non-momentum conserving electron-electron scattering in the clean limit,^{42,43,34} are both known to yield $L_{th} \sim T^{-1}$. Their coexistence with the $T^{-1/2}$ exponent rule can yield an intermediate decay exponent. Decay exponents exceeding $p = 0.5$ have been reported in previous measurements on $Pb_{1-x}Sn_xSe$ with lower mobility and high carrier density,^{44,15} ruling out a

mechanism that is highly density dependent and favoring electron-phonon scattering as a possible explanation. A saturation of L_{th} is also observed at 2K, however, more measurements at low temperature are needed to further understand this mechanism.

Comparison with previous work

Lastly, table 2 shows a systematic comparison between our results and transport parameters extracted from previous work on TCIs and trivial IV-VI systems. We highlight that the mobility is at least an order of magnitude higher than in any previously reported TCI single QW and the carrier density is a factor of 2 to 4 lower than in $\text{Pb}_{1-x}\text{Sn}_x\text{Se}$ on STO (see table 2). A dramatic improvement of the transport properties of TCI single QWs is thus achieved approaching what has been realized in multiquantum wells and bulk materials.^{16,45} While elastic scattering is dramatically reduced compared to other works, the inelastic scattering length is comparable to what was recently measured by Kazakov et al.¹⁵ This corroborates the reasoning that phonons or morphological defects (domain boundaries, surface scattering...) play a role in limiting quantum coherence in $\text{Pb}_{1-x}\text{Sn}_x\text{Se}$.

| Reference | Density [cm^{-2}] | Mobility [cm^2/Vs] | Thouless length [nm] |
|--|--|--------------------------------------|-----------------------------------|
| This work – QW-4 | 1.3×10^{13} | 8600 | 1250 (3K) – WS 1750 (3K) – HLN |
| This work – QW-3 | 6.6×10^{12} | 11300 | |
| ⁸ SnTe (40nm) on BaF_2 | $>4 \times 10^{13}$ | <800 | 500 (2K) |
| ⁴⁴ $\text{Pb}_{1-x}\text{Sn}_x\text{Se}$ on STO | 2×10^{13} | <100 | 350 (2K) |
| ⁹ SnTe (ultrathin) on STO | 5×10^{14} | <100 | 200 (1.8K) |
| ¹⁰ SnTe on BaF_2 | $5 \times 10^{12}, 1.7 \times 10^{14}$ | 400, 900 | 200, 635 (4K) |
| ¹⁵ $\text{Pb}_{0.76}\text{Sn}_{0.24}\text{Se}$ (50nm) | 8.5×10^{13} | 930 | 1830 (1.5K) |

Table 2. Carrier density, mobility and Thouless length obtained from different works on TCI QWs.

Conclusion

In summary, we have grown high-quality $\text{Pb}_{0.7}\text{Sn}_{0.3}\text{Se}/\text{Pb}_{0.9}\text{Eu}_{0.1}\text{Se}$ single quantum wells and reached a regime where the HLN model is no longer valid. We implement the WS model to extract the inelastic scattering parameters, which gives us access to the inelastic scattering time, in addition to the Thouless length. Although previously considered for HgTe,^{27,46} models that are valid beyond the diffusion limit have not yet been employed in 3D topological insulators. Further theoretical insight is needed to further develop such models, taking into account valley degeneracy and spin-momentum locking. While our coherence time exceeds 100ps at 3K, we argue that electron-phonon scattering or morphological defects play a key role in limiting it.

Despite this limitation, our work has achieved needed progress making single TCI QWs with high mobility available for future studies at high magnetic field. Even more importantly, we achieve this in a structure that hosts a type-I topological band alignment (Fig. 1(a)), in contrast with the broken gap alignment of the SnTe-PbTe interface.⁴⁷ With this ideal band alignment and the improved transport characteristics realized in a single well, our work enables future transport measurements in the Hall quantized regime of TCIs⁵⁴ and in the second order topological insulating regime predicted in strained TCIs.⁴⁸

Appendix A. Band structure k.p envelope function model

We use a k.p envelope function model to compute the band structure of our TCI QW.^{49,50,16} The band structure of $\text{Pb}_{1-x}\text{Sn}_x\text{Se}$ in the bulk is comprised of the conduction band L_6^- and the valence band L_6^+ which have opposite parity.⁵¹ The heterostructure is comprised of a QW of $\text{Pb}_{0.7}\text{Sn}_{0.3}\text{Se}$ sandwiched between two layers of $\text{Pb}_{0.9}\text{Eu}_{0.08}\text{Se}$ grown along the [111] direction (referred to as the \hat{z} direction) as shown in Fig. 1(a). The Sn/Pb ratio is fixed at $x=0.3$ as determined from X-ray diffraction measurements on the QW and control bulk samples. The well hosts an inverted band structure while the barrier hosts non-inverted levels.^{52,53,17,26}

In this structure, a quasi-symmetric potential barrier of magnitude V confines electrons in the well.¹⁶ Since the band gap ($-\varepsilon_A$) of the well material is negative, an inverted junction is created at the interfaces and topological Dirac states emerge at this interface. The 4-band k.p envelop function model described here is used to compute the band dispersion of the topological and trivial states of the QW.¹⁶ The thickness of the well along the growth axis is d and the point $z = 0$ is chosen in the middle of the well so that the confining potential is an even function. In the setup illustrated in Fig. 1(a), zero energy is taken to be at the bottom of the bulk conduction band. If we consider only the nearest bands and spin and neglect far bands the Hamiltonian can be expressed in the basis $|L_6^+, \uparrow\rangle, |L_6^+, \downarrow\rangle, |L_6^-, \uparrow\rangle, |L_6^-, \downarrow\rangle$ ⁵¹ as:

$$\hat{H} = \begin{pmatrix} V_- & 0 & \hbar v_z k_z & \hbar v_\perp (k_x - ik_y) \\ 0 & V_- & \hbar v_\perp (k_x + ik_y) & -\hbar v_z k_z \\ \hbar v_z k_z & \hbar v_\perp (k_x - ik_y) & -\varepsilon_A + V_+ & 0 \\ \hbar v_\perp (k_x + ik_y) & -\hbar v_z k_z & 0 & -\varepsilon_A + V_+ \end{pmatrix}.$$

The diagonal terms contain the step functions defined as $V_\pm(z) = \pm V$ for z outside the well, else $V_\pm(z) = 0$. \hat{H} thus depends on the energy parameters V and ε_A , the wavevector $\mathbf{k} = (k_x, k_y, k_z)$, and the empirically determined Dirac velocity v_D . Note that v_z is the out-of-plane velocity and v_\perp is the in-plane velocity, assumed to be equal, and that these values are closely related to the Kane matrix element P according to $v_z = P/m_0$.

The potential barrier in the \hat{z} results in confinement such that k_z is not a good quantum number. Conversely, the particle is free in the \hat{x} and \hat{y} direction so the other two components of the wavevector are good quantum numbers. We proceed by fixing $k_x = k_y = 0$. The simplified Hamiltonian is then

$$\hat{H} = \begin{pmatrix} V_- & 0 & -i\hbar v_z \partial_z & 0 \\ 0 & V_- & 0 & i\hbar v_z \partial_z \\ -i\hbar v_z \partial_z & 0 & -\varepsilon_A + V_+ & 0 \\ 0 & i\hbar v_z \partial_z & 0 & -\varepsilon_A + V_+ \end{pmatrix}.$$

This matrix is independent of x and y , so that in the eigenvalue equation we cancel out all but the z dependent parts of the L_6^+ and L_6^- envelope functions, $\chi_1(z)$ and $\chi_2(z)$. The potential is even in z ,

ensuring that the $\chi(z)$ functions in the well are alternatively even and odd. Outside the well, we require they take the evanescent form $\chi(z) = Be^{-\rho(|z|-d/2)}$ so that the wavefunction will be normalizable. Furthermore, since all the nonzero matrix elements are purely $\langle \uparrow | \hat{H} | \uparrow \rangle$ or $\langle \downarrow | \hat{H} | \downarrow \rangle$, we may separate the problem by spin into

$$\hat{H}_{\downarrow} \vec{\Psi}_n = E \vec{\Psi}_n \text{ for } \hat{H}_{\downarrow} = \begin{pmatrix} V_- & -i\hbar v_z \partial_z \\ -i\hbar v_z \partial_z & -\varepsilon_A + V_+ \end{pmatrix} \text{ and } \vec{\Psi}_n = \begin{pmatrix} \chi_1^n \\ \chi_2^n \end{pmatrix}$$

$$\text{and } \hat{H}_{\uparrow} \vec{\varphi}_n = E \vec{\varphi}_n \text{ for } \hat{H}_{\uparrow} = \begin{pmatrix} V_- & i\hbar v_z \partial_z \\ i\hbar v_z \partial_z & -\varepsilon_A + V_+ \end{pmatrix} \text{ and } \vec{\varphi}_n = \begin{pmatrix} \chi_1^n \\ -\chi_2^n \end{pmatrix}$$

Here the index n refers to the energy level. Enforcement of the appropriate boundary conditions at $z = \frac{d}{2}$ for the even case $\chi_1 = A \cos(k_z z)$ gives two equations,

$$A \cos\left(k_z \frac{d}{2}\right) = B \quad \text{and} \quad \frac{-A k_z}{-E - \varepsilon_A} \sin\left(\frac{k_z d}{2}\right) = \frac{-B \rho}{-E - \varepsilon_A + V}$$

which can be divided to obtain a single equation which can be solved for E ,

$$\tan\left(\frac{k_z d}{2}\right) = \frac{\rho(E + \varepsilon_A)}{k_z(E + \varepsilon_A - V)} \quad \text{for } \chi_1 \text{ even.} \quad \text{Eq. (1)}$$

This process is easily repeated to obtain three additional equations,

$$\cotan\left(\frac{k_z d}{2}\right) = -\frac{\rho(E + \varepsilon_A)}{k_z(E + \varepsilon_A - V)} \quad \text{for } \chi_1 \text{ odd,} \quad \text{Eq. (2)}$$

$$\tanh\left(\frac{-ik_z d}{2}\right) = \frac{\rho(E + \varepsilon_A)}{ik_z(E + \varepsilon_A - V)} \quad \text{for } \chi_1 \text{ even and } k_z \text{ imaginary,} \quad \text{Eq. (3)}$$

$$\text{and } \cotanh\left(\frac{-ik_z d}{2}\right) = \frac{\rho(E + \varepsilon_A)}{ik_z(E + \varepsilon_A - V)} \quad \text{for } \chi_1 \text{ odd and } k_z \text{ imaginary.} \quad \text{Eq. (4)}$$

The appropriate wavenumbers are given by $k_z = \frac{1}{\hbar v_z} \sqrt{E(E + \varepsilon_A)}$ inside the well and $\rho = \frac{1}{\hbar v_z} \sqrt{(E + V)(-E - \varepsilon_A + V)}$ inside the barrier.

Note that Eq. 3 and 4 are valid in the energy regime $-\varepsilon_A < E < 0$ and each can admit only one solution representing the topological interface states of the system. Eq. 1 and 2 are valid at any other energy and represents the confined levels of the QW. This approach is identical to the one utilized in ref.¹⁶ to determine the energy levels of $\text{Pb}_{1-x}\text{Sn}_x\text{Se}$ QW.

The energy dispersion of the QW states is needed to determine the diffusion constant. A systematic perturbation scheme is usually applied to the QW states to determine the dispersion.¹⁶ The result is evidently a set of massive Dirac bands and one massless Dirac state representing the topological state. In ref ¹⁶, one can notice that the Dirac velocity that determines the dispersion of the QW states is almost equal to that of the bulk bands.¹⁶ Therefore, we can justify, a posteriori, simply using

$$E_i(k) = \sqrt{\Delta_i^2 + (\hbar v_D k)^2}$$

With $v_D \approx 3.95 \times 10^5 \text{ m/s}$ to compute the energy dispersion of all the QW levels including the topological interface states. Δ_i is the energy separation between each subband edge and the midgap. It is equal to 0 for the topological states. Using the following input parameters for the model, $d = 50 \text{ nm}$, $\mathcal{E}_A = -100 \text{ meV}$, $v_D = v_z = 3.95 \times 10^5 \text{ m/s}$ ²⁶ and $V = V^{+/-} = \pm 250 \text{ meV}$ ⁵⁴, we obtain the band dispersion shown in Fig. 6.

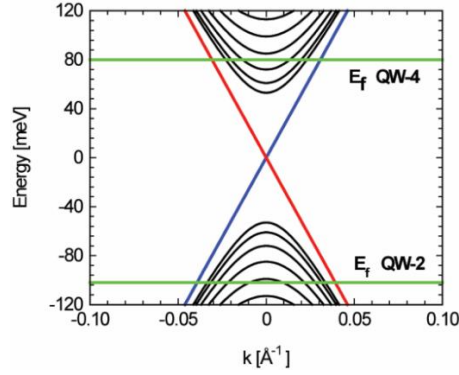


FIG 6. Band structure computed using the k.p formalism and the band alignment shown in Fig. 1(a). QW subbands are shown in black and the topological interface states is shown in red and blue. The Fermi level position of QW-2 and QW-4 is shown in green. The bands are offset compared to the model parameters to have the midgap lie at zero energy.

Appendix B. The diffusion constant in a multiband system

In order to determine the diffusion constant in a multiband system, a good knowledge of the band structure is required. This is a consequence of the fact that

$$D = \frac{1}{2} v_f^2 \tau$$

There v_f is the Fermi velocity. From our measured carrier density, we are able to determine the Fermi energy with fair reliability. The scattering time τ can be obtained directly from the mobility. Below, we show a detailed description of how D is determined.

Given the band structure calculated above, we can calculate Fermi energy E_f based on measured carrier density n by

$$E_i(k) = \sqrt{\Delta_i^2 + (\hbar v_D k)^2}$$

$$n_i = \frac{k^2}{2\pi} \quad \text{with} \quad n_{\text{experimental}} = 4 \sum n_i$$

The factor of 4 is due to the 4-fold valley degeneracy of TCIs. i is the subband index. The effective mass m is energy dependent in non-parabolic and Dirac semiconductors. m at the Fermi energy can be calculated from:

$$\frac{1}{m} = \frac{2}{\hbar^2} \frac{dE}{d(k^2)} = \frac{v_D^2}{E_f}$$

We can then calculate effective Fermi velocity at E_f for each subband simply using:

$$v_i(k) = \frac{\hbar k}{m}$$

The effective Fermi velocity is then a weighted average velocity over all partially occupied subbands

$$v_f = \sum \frac{v_i \cdot N_i}{N_{tot}}$$

Here N_i is the density of states and v_i the Fermi velocity at the Fermi level for each partially occupied band, and N_{tot} is the sum over all density of states, as discussed in previous experimental work on HgTe QW²⁷ and in general for any multiband system.²⁸ IV-VI materials host a nearly-ideal massive Dirac dispersion. v_f is then a simple average over all partially occupied bands.

The elastic scattering time can now be extracted from the experimental measurement of the mobility:

$$\tau_e = \frac{m\mu}{e}$$

We can now determine $L_e = v_f \tau_e$ and the diffusion constant D . We use this computed L_e to determine B_{tr} as shown in table 1. For QW-4, we find the effective mass $m \approx 0.089m_0$ and $v_f \approx (2.7 \pm 0.2) \times 10^5 m/s$. From the mobility, we get $\tau_e \approx 0.42 ps$, so elastic scattering length $L_e = v_f \tau_e \approx (114 \pm 8) nm$ and $D \approx (160 \pm 24) cm^2/s$. For QW-2, $m \approx 0.13m_0$ and $v_f \approx (2.8 \pm 0.2) \times 10^5 m/s$. The Hall mobility thus gives, $\tau_e \approx 0.18 ps$, $L_e = (52 \pm 4) nm$ and $D = (73 \pm 10) cm^2/s$.

The uncertainty on v_f is dominantly due to the uncertainty on the composition of the well, i.e. the bulk band gap on $Pb_{1-x}Sn_xSe$ layer (with $x=0.3 \pm 0.03\%$).

Appendix C. Transmission electron microscopy

Transmission electron microscopy measurements are performed on QW-4. Energy dispersive X-ray (EDX) maps (Fig. 7(a-c)) show the distribution of Sn, Eu and Pb across the heterostructure. It is evident that Sn is concentrated in well. The EDX measurements allows us to estimate the position of the barrier/well interface. A zoom-in (Fig. 7(d)) at an interface confirms that the two barriers and the well are indeed pseudomorphic.

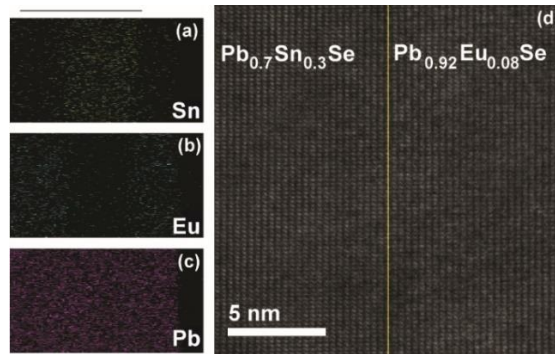


FIG 7. (a) EDX maps of QW-4 in the vicinity of the well. (b) Real space TEM image of QW top interface.

Acknowledgements

The work is supported by NSF-DMR 1905277 and partly by a seed grant from Notre Dame Nanoscience and Technology (NDnano). The Material Characterization Facility is funded by the Sustainable Energy Initiative (SEI), which is part of the Center for Sustainable Energy at Notre Dame (ND Energy). We also acknowledge support from the Notre Dame Integrated Imaging Facility.

References

- [1] P. Dziawa, B. J. Kowalski, K. Dybko, R. Buczko, A. Szczerbakow, M. Szot, E. Łusakowska, T. Balasubramanian, B. M. Wojek, M. H. Berntsen, O. Tjernberg, and T. Story, "Topological crystalline insulator states in $\text{Pb}(1-x)\text{Sn}(x)\text{Se}$ ". *Nat. Mater.* **11**, 1023 (2012).
- [2] T. H. Hsieh, H. Lin, J. Liu, W. Duan, A. Bansil, and L. Fu, "Topological crystalline insulators in the SnTe material class". *Nat. Commun.* **3**, 982 (2012).
- [3] Y. Okada, M. Serbyn, H. Lin, D. Walkup, W. Zhou, C. Dhital, M. Neupane, S. Xu, Y. J. Wang, R. Sankar, F. Chou, A. Bansil, M. Z. Hasan, S. D. Wilson, L. Fu, and V. Madhavan, "Observation of Dirac node formation and mass acquisition in a topological crystalline insulator". *Science*. **341**, 1496 (2013).
- [4] I. Sodemann, Z. Zhu, and L. Fu, "Quantum Hall Ferroelectrics and Nematics in Multivalley Systems". *Phys. Rev. X*. **7**, 041068 (2017).
- [5] X. Li, F. Zhang, and A. H. H. MacDonald, "SU(3) Quantum Hall Ferromagnetism in SnTe". *Phys. Rev. Lett.* **116**, 026803 (2016).
- [6] C. Fang, M. J. Gilbert, and B. A. Bernevig, "Large-chern-number quantum anomalous hall effect in thin-film topological crystalline insulators". *Phys. Rev. Lett.* **112**, 046801 (2014).
- [7] U. A. Mengui, E. Abramof, P. H. O. Rappl, and A. Y. Ueta, "Characterization of SnTe films grown by molecular beam epitaxy". *Brazilian J. Phys.* **36**, 324 (2006).
- [8] B. A. Assaf, F. Katmis, P. Wei, B. Satpati, Z. Zhang, S. P. Bennett, V. G. Harris, J. S. Moodera, and D. Heiman, "Quantum coherent transport in SnTe topological crystalline insulator thin films". *Appl. Phys. Lett.* **105**, 102108 (2014).
- [9] K. Zou, S. D. Albright, O. E. Dagdeviren, M. D. Morales-Acosta, G. H. Simon, C. Zhou, S. Mandal, S. Ismail-Beigi, U. D. Schwarz, E. I. Altman, F. J. Walker, and C. H. Ahn, "Revealing surface-state transport in ultrathin topological crystalline insulator SnTe films". *APL Mater.* **7**, 051106 (2019).
- [10] R. Akiyama, K. Fujisawa, T. Yamaguchi, R. Ishikawa, and S. Kuroda, "Two-dimensional quantum transport of multivalley (111) surface state in topological crystalline insulator SnTe thin films". *Nano Res.* **9**, 490 (2016).
- [11] M. M. Olver, J. Z. Pastalan, S. E. Romaine, B. B. Goldberg, G. Springholz, G. Ihninger, and G. Bauer, "The observation of the integral quantum Hall effect in $\text{PbTe}/\text{Pb}_{1-x}\text{Eu}_x\text{Te}$ quantum well structures". *Solid State Commun.* **89**, 693 (1994).
- [12] V. A. Chitta, W. Desrat, D. K. Maude, B. A. Piot, N. F. Oliveira, P. H. O. Rappl, A. Y. Ueta, and E. Abramof, "Multivalley transport and the integer quantum Hall effect in a PbTe quantum well". *Phys. Rev. B*. **72**, 195326 (2005).
- [13] J. Melngailis, T. C. Harman, and W. C. Kernan, "Shubnikov-de Hass Measurements in $\text{Pb}_{1-x}\text{Sn}_x\text{Se}$ ". *Phys. Rev. B*. **5**, 2250 (1972).

- [14] B. A. Assaf, T. Phuphachong, E. Kampert, V. V. Volobuev, P. S. Mandal, J. Sánchez-Barriga, O. Rader, G. Bauer, G. Springholz, L. A. De Vaultchier, and Y. Guldner, "Negative Longitudinal Magnetoresistance from the Anomalous $N=0$ Landau Level in Topological Materials". *Phys. Rev. Lett.* **119**, 106602 (2017).
- [15] A. Kazakov, W. Brzezicki, T. Hyart, B. Turowski, J. Polaczyński, Z. Adamus, M. Aleszkiewicz, T. Wojciechowski, J. J. Domagała, A. Varykhalov, G. Springholz, T. Wojtowicz, V. V. Volobuev, and T. Dietl, "Mirror-symmetry protected quantization of Berry phases and resulting magnetoresistance across the topological transition in $\text{Pb}_{1-x}\text{Sn}_x\text{Se}$ ". (2020).
- [16] G. Krizman, B. A. Assaf, T. Phuphachong, G. Bauer, G. Springholz, G. Bastard, R. Ferreira, L. A. de Vaultchier, and Y. Guldner, "Tunable Dirac interface states in topological superlattices". *Phys. Rev. B.* **98**, 075303 (2018).
- [17] G. Bauer, in *Narrow Gap Semicond. Phys. Appl. Proceeding Int. Summer Sch.*, edited by W. Zawadzki (Springer Berlin Heidelberg, Berlin, Heidelberg, 1980), pp. 427–446.
- [18] H. Z. Lu, J. Shi, and S. Q. Shen, "Competition between weak localization and antilocalization in topological surface states". *Phys. Rev. Lett.* **107**, 1 (2011).
- [19] P. Adroguer, W. E. Liu, D. Culcer, and E. M. Hankiewicz, "Conductivity corrections for topological insulators with spin-orbit impurities: Hikami-Larkin-Nagaoka formula revisited". *Phys. Rev. B.* **92**, 241402 (2015).
- [20] G. M. Stephen, O. A. Vail, J. Lu, W. A. Beck, P. J. Taylor, and A. L. Friedman, "Weak Antilocalization and Anisotropic Magnetoresistance as a Probe of Surface States in Topological $\text{Bi}_2\text{TeSe}_{3-x}$ Thin Films". *Sci. Rep.* **10**, 4845 (2020).
- [21] G. Tkachov and E. M. Hankiewicz, "Weak antilocalization in HgTe quantum wells and topological surface states: Massive versus massless Dirac fermions". *Phys. Rev. B.* **84**, 035444 (2011).
- [22] S. Hikami, A. I. Larkin, and Y. Nagaoka, "Spin-Orbit Interaction and Magnetoresistance in the Two Dimensional Random System". *Prog. Theor. Phys.* **63**, 707 (1980).
- [23] H. P. Wittmann and A. Schmid, "Anomalous magnetoconductance beyond the diffusion limit". *J. Low Temp. Phys.* **69**, 131 (1987).
- [24] P. S. Mandal, G. Springholz, V. V. Volobuev, O. Caha, A. Varykhalov, E. Golias, G. Bauer, O. Rader, and J. Sánchez-Barriga, "Topological quantum phase transition from mirror to time reversal symmetry protected topological insulator". *Nat. Commun.* **8**, 968 (2017).
- [25] A. Y. Ueta, G. Springholz, F. Schinagl, G. Marschner, and G. Bauer, "Doping studies for molecular beam epitaxy of PbTe and $\text{Pb}_{1-x}\text{EuxTe}$ ". *Thin Solid Films.* **306**, 320 (1997).
- [26] G. Krizman, B. A. Assaf, T. Phuphachong, G. Bauer, G. Springholz, L. A. de Vaultchier, and Y. Guldner, "Dirac parameters and topological phase diagram of $\text{Pb}_{1-x}\text{Sn}_x\text{Se}$ from magnetospectroscopy". *Phys. Rev. B.* **98**, 245202 (2018).
- [27] G. M. Minkov, A. V. Germanenko, O. E. Rut, A. A. Sherstobitov, S. A. Dvoretzki, and N. N. Mikhailov, "Weak antilocalization of holes in HgTe quantum wells with a normal energy spectrum". *Phys. Rev. B.* **91**, 205302 (2015).
- [28] D. Rainer and G. Bergmann, "Multiband effects in weak localization". *Phys. Rev. B.* **32**, 3522

(1985).

- [29] M. L. Peres, H. S. Monteiro, V. a. Chitta, S. de Castro, U. a. Mengui, P. H. O. Rappl, N. F. Oliveira, E. Abramof, and D. K. Maude, "Experimental investigation of spin-orbit coupling in n-type PbTe quantum wells". *J. Appl. Phys.* **115**, 093704 (2014).
- [30] M. Rudolph and J. J. Heremans, "Spin-orbit interaction and phase coherence in lithographically defined bismuth wires". *Phys. Rev. B.* **83**, 205410 (2011).
- [31] A. A. Taskin, S. Sasaki, K. Segawa, and Y. Ando, "Manifestation of Topological Protection in Transport Properties of Epitaxial Bi₂Se₃ Thin Films". *Phys. Rev. Lett.* **109**, 066803 (2012).
- [32] H. Steinberg, J.-B. Laloë, V. Fatemi, J. S. Moodera, and P. Jarillo-Herrero, "Electrically tunable surface-to-bulk coherent coupling in topological insulator thin films". *Phys. Rev. B.* **84**, 233101 (2011).
- [33] J. Wang, A. M. DaSilva, C.-Z. Chang, K. He, J. K. Jain, N. Samarth, X.-C. Ma, Q.-K. Xue, and M. H. W. Chan, "Evidence for electron-electron interaction in topological insulator thin films". *Phys. Rev. B.* **83**, 245438 (2011).
- [34] G. Bergmann, "Weak Localization in Thin Films". *Phys. Rep.* **107**, 1 (1984).
- [35] B. A. Assaf, T. Cardinal, P. Wei, F. Katmis, J. S. Moodera, and D. Heiman, "Linear magnetoresistance in topological insulator thin films: Quantum phase coherence effects at high temperatures". *Appl. Phys. Lett.* **102**, 012102 (2013).
- [36] S. McPhail, C. E. Yasin, A. R. Hamilton, M. Y. Simmons, E. H. Linfield, M. Pepper, and D. A. Ritchie, "Weak localization in high-quality two-dimensional systems". *Phys. Rev. B.* **70**, 245311 (2004).
- [37] G. M. Minkov, A. V. Germanenko, V. A. Larionova, S. A. Negashev, and I. V. Gornyi, "Analysis of negative magnetoresistance: Statistics of closed paths. I. Theory". *Phys. Rev. B.* **61**, 13164 (2000).
- [38] B. L. Altshuler, A. G. Aronov, and D. E. Khmelnitsky, "Effects of electron-electron collisions with small energy transfers on quantum localisation". *J. Phys. C Solid State Phys.* **15**, 7367 (1982).
- [39] H. Fukuyama, "A Note on Inelastic Scattering Time in Two-Dimensional Weakly Localized Regime". *J. Phys. Soc. Japan.* **53**, 3299 (1984).
- [40] J. J. Lin and J. P. Bird, "Recent experimental studies of electron dephasing in metal and semiconductor mesoscopic structures". *J. Phys. Condens. Matter.* **14**, (2002).
- [41] D. Belitz and S. Das Sarma, "Inelastic phase-coherence time in thin metal films". *Phys. Rev. B.* **36**, 7701 (1987).
- [42] H. Fukuyama and E. Abrahams, "Inelastic scattering time in two-dimensional disordered metals". *Phys. Rev. B.* **27**, 5976 (1983).
- [43] E. Abrahams, P. W. Anderson, P. A. Lee, and T. V. Ramakrishnan, "Quasiparticle lifetime in disordered two-dimensional metals". *Phys. Rev. B.* **24**, 6783 (1981).
- [44] C. Zhang, Y. Liu, X. Yuan, W. Wang, S. Liang, and F. Xiu, "Highly tunable Berry phase and ambipolar field effect in topological crystalline insulator Pb(1-x)Sn(x)Se.". *Nano Lett.* **15**, 2161 (2015).
- [45] Y. Wang, G. Luo, J. Liu, R. Sankar, N.-L. Wang, F. Chou, L. Fu, and Z. Li, "Observation of ultrahigh

- mobility surface states in a topological crystalline insulator by infrared spectroscopy". *Nat. Commun.* **8**, 366 (2017).
- [46] G. M. Minkov, A. V. Germanenko, O. E. Rut, A. A. Sherstobitov, S. A. Dvoretzki, and N. N. Mikhailov, "Weak antilocalization in HgTe quantum wells with inverted energy spectra". *Phys. Rev. B.* **85**, 235312 (2012).
 - [47] F. Wei, C.-W. Liu, D. Li, C.-Y. Wang, H.-R. Zhang, J.-R. Sun, X. P. A. Gao, S. Ma, and Z. Zhang, "Broken mirror symmetry tuned topological transport in PbTe/SnTe heterostructures". *Phys. Rev. B.* **98**, 161301 (2018).
 - [48] F. Schindler, A. M. Cook, M. G. Vergniory, Z. Wang, S. S. P. Parkin, B. A. Bernevig, and T. Neupert, "Higher-order topological insulators". *Sci. Adv.* **4**, eaat0346 (2018).
 - [49] G. Bastard, *Wave Mechanics Applied to Semiconductor Heterostructures*. Les éditions de physique (Les Ulis, France, 1996).
 - [50] G. Bastard, "Superlattice band structure in the envelope-function approximation". *Phys. Rev. B.* **24**, 5693 (1981).
 - [51] D. L. Mitchell and R. F. Wallis, "Theoretical energy-band parameters for the lead salts". *Phys. Rev.* **151**, 581 (1966).
 - [52] A. J. Strauss, "Inversion of conduction and valence bands in $\text{Pb}_{1-x}\text{Sn}_x\text{Se}$ alloys". *Phys. Rev.* **157**, 608 (1967).
 - [53] B. M. Wojek, P. Dziawa, B. J. Kowalski, A. Szczerbakow, a. M. Black-Schaffer, M. H. Berntsen, T. Balasubramanian, T. Story, and O. Tjernberg, "On the nature of the band inversion and the topological phase transition in $(\text{Pb},\text{Sn})\text{Se}$ ". *Phys. Rev. B.* **90**, 161202 (2014).
 - [54] M. Simma, G. Bauer, and G. Springholz, "Band alignments and strain effects in PbTe/ $\text{Pb}_{1-x}\text{SrxTe}$ and PbSe/ $\text{Pb}_{1-x}\text{SrxSe}$ quantum-well heterostructures". *Phys. Rev. B.* **90**, 195310 (2014).